Inorganica Chimica Acta 572 (2024) 122310

Contents lists available at ScienceDirect

Inorganica Chimica Acta

journal homepage: www.elsevier.com/locate/ica

Research paper

Synthesis of anhydrous lanthanum acetate. Analysis of it's structural, thermal and electronic properties

A.S. Oreshonkov [a,b,*], N.O. Azarapin [c], A.P. Tyutyunnik [d], D.V. Pankin [e], I.A. Razumkova [c]

[a] Laboratory of Molecular Spectroscopy, Kirensky Institute of Physics, Federal Research Center KSC SB RAS, 660036 Krasnoyarsk, Russia
[b] School of Engineering and Construction, Siberian Federal University, 660041 Krasnoyarsk, Russia
[c] Department of Inorganic and Physical Chemistry, Tyumen State University, Tyumen 625003, Russia
[d] Institute of Solid State Chemistry UB RAS, Yekaterinburg, Russia
[e] Center for Optical and Laser Materials Research, Saint-Petersburg State University, Saint-Petersburg 199034, Russia

ARTICLE INFO

Keywords:
Anhydrous acetate
Rare-earth
Electronic structure
Optical properties
Deep UV

ABSTRACT

Acetate complexes of rare earth elements are extensively studied compounds known for their diverse properties and potential applications and lanthanum acetate hydrate is commercially available. In this work, a powdered anhydrous lanthanum acetate ($La(CH_3COO)_3$) sample was prepared by dissolving lanthanum oxide (La_2O_3) in an excess of acetic acid (CH_3COOH) and distilled water (H_2O), followed by direct evaporation at 150 °C. The decomposition of $La(CH_3COO)_3$ was studied, showing initiation around 300 °C and conclusion at ≥700 °C, with four distinct thermal events (I–IV) of mass loss. Gas phase identification revealed acetone and carbon dioxide as decomposition products, indicating pyrolytic decarboxylation. The final thermal effect (IV) is linked to the decomposition of $La_2O_2CO_3$ to La_2O_3. The DFT refinement of atomic coordinates of hydrogen atoms, which were unavailable from experiment, was successfully performed. Obtained structural data was checked using vibrational spectroscopy method. The calculated electronic band structure of $La(CH_3COO)_3$ indicates it as an indirect wide band gap material with values of direct transition close to indirect. The optical bandgap is found to be 5.49 eV, suggesting that the charge transfer in $La(CH_3COO)_3$ can be optically activated with wavelengths shorter than 226 nm, which falls within the deep UV (DUV) region.

1. Introduction

At present, rare-earth elements have already accumulated in household garbage in enough quantities for considering urban mining [1–5]. The drive to minimize humanity's carbon footprint and maintain ecological equilibrium suggests that the utilization of complexes of rare earth elements should be carried out through non-toxic and environmentally safe methods [6,7]. Oxalate extraction methods, along with the utilization of organic acids and MOF-type compounds are suitable for extracting rare earth elements [8]. Additionally, the extraction of rare earth elements using lanmodulin has recently been explored [9–11].

Acetate complexes of rare earth elements are part of the extensively studied classes of coordination compounds. Centrosymmetric binuclear coordination compounds of rare earth elements with acetate bridges are known to exhibit partial cytotoxicity towards MCF-7 cells (breast cancer cell line) [12]. Lanthanum has been used to reduce serum phosphorus levels in patients with chronic renal disease and hyperphosphatemia. Lanthanum acetate has demonstrated effective inhibition of vascular calcification pathogenesis [13]. Acetates of rare earth elements, along with their respective complexes, exhibit luminescent properties [14], magnetic behavior [15], and catalytic activity [16]. Lanthanum-based compounds exhibit semiconductor properties, too [17,18]. Lanthanum salts serve as catalysts [16,19] and find applications in the production of fuel cells based on high-entropy compounds [20,21], as well as in the manufacturing of ZBLAN (The ZrF_4-BaF_2-LaF_3-AlF_3-NaF optical fiber) [22]. Among the other members of the anhydrous rare-earth (RE) element acetate family, $Ce(CH_3COO)_3$ can be used to synthesize catalysts such as Ce-HZSM-5, which has proven to be a promising compound for AsH_3 removal [23]. Praseodymium acetate ($Pr(CH_3COO)_3$) was used to synthesize $Pr_2Sn_2O_7$ nanospheres with diameters ranging from 20 to 50 nm, which were found to be composed of nanoparticles with average sizes of 3–5 nm [24]. We are compelled to conclude that information on other anhydrous representatives of this acetate family is extremely scarce. At the same time, this opens a potential for applications related

* Corresponding author at: Laboratory of Molecular Spectroscopy, Kirensky Institute of Physics, Federal Research Center KSC SB RAS, 660036 Krasnoyarsk, Russia.
E-mail address: oreshonkov@iph.krasn.ru (A.S. Oreshonkov).

https://doi.org/10.1016/j.ica.2024.122310
Received 16 May 2024; Received in revised form 30 July 2024; Accepted 8 August 2024
Available online 8 August 2024

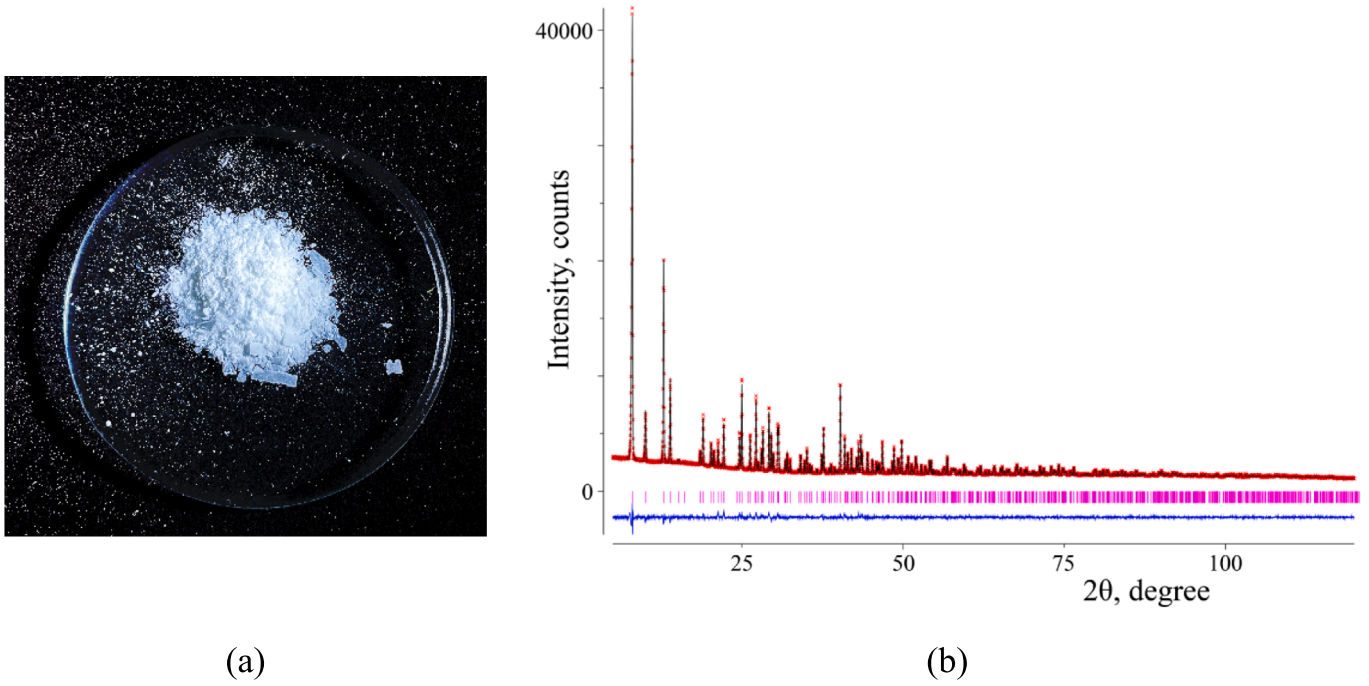

Fig. 1. Photo (a) and difference Rietveld plot (b) of $La(CH_3COO)_3$ powder (black line – calculated pattern, red crosses – experimental pattern, blue line – difference, magenta tick marks – Bragg positions of reflections).

to the presence of rare earth ions in the structure, which may indicate possible use as luminescent or magnetic materials.

The crystal structure of anhydrous rare-earth (RE) elements acetates varies according to the RE ion as follows: La-Ce – trigonal structure ($R\bar{3}$) [25], Pr – tetragonal structure ($P\bar{4}2_1c$) [26], Nd – monoclinic structure ($P2_1/a$) [27], Sm-Er and Y – monoclinic structure ($C2/c$) [28], Tm-Lu – orthorhombic structure ($Ccm2_1$) [28], and Sc – hexagonal structure ($P6_3/mcm$) [29].

The $La(CH_3COO)_3$ monocrystal was synthesized by Meyer et al. [25] and as was shown above, this material crystallizes in the trigonal $R\bar{3}$ space group. The unit cell parameters of ($La(CH_3COO)_3$) were determined at room temperature as a = 22.030(5) Å, c = 9.871(3) Å. Thermal stability of lanthanum acetate monocrystal and degradation mechanism in an inert or oxygen environment were studied in several works [30–32]. Thermal decomposition of lanthanum acetate hydrate with forming of La_2O_3 as a final product was studied in work of Hussein et al. [30].

This paper focuses on the investigation of anhydrous lanthanum acetate ($La(CH_3COO)_3$) powder, including refining the positions of hydrogen within the crystalline structure, studying its electronic structure, and determining it's thermal stability limit.

2. Materials and methods

A powdered sample of lanthanum acetate ($La(CH_3COO)_3$) was obtained by dissolving lanthanum oxide (La_2O_3) in an excess of acetic acid (CH_3COOH) and distilled water (H_2O) followed by direct evaporation at 150 °C. The following high-purity reagents were used as the starting materials: La_2O_3 (99,99 %, ultrapure, TDM-96 Ltd. Russia), acetic acid ($w(CH_3COOH)$ = 70 %, ultrapure, Vekton Ltd., Russia).

The X-ray powder diffraction (XRD) data were collected at room temperature on a STADI-P STOE (Germany) diffractometer in the transmission geometry, with a linear mini-PSD detector, using CuKα1 radiation in the 2θ range from 5 to 120°, with the step of 0.02°. The crystal structure refinement was carried out with the GSAS program suite, using XRPD data [33]. The peak profiles were fitted with a pseudo-Voigt function, $I(2\theta) = x \times L(2\theta) + (1 - x) \times G(2\theta)$ (where L and G are the Lorentzian and Gaussian parts, respectively). The peak width angular dependence was described by the relation $(FWHM)^2 = Utg^2\theta + Vtg\theta + W$. The background level was described by a combination of 36-order Chebyshev polynomials. The absorption correction function for a flat plate sample in the transmission geometry was applied.

The CASTEP [34] code was used for the complete optimization of structural parameters and calculation of the electronic structure of $La(CH_3COO)_3$. The local density approximation [35], based on the Perdew and Zunger parameterization [36] of the numerical results of Ceperley and Alder [37], was employed. Structural parameters were relaxed until the maximum forces and stress were below 0.01 eV/Å and 0.02 GPa, respectively. Norm-conserving pseudopotentials and a plane-wave cut-off of 830 eV were applied. The reciprocal space of the primitive cell was sampled using a 3 × 3 × 3 Monkhorst–Pack k-mesh.

The Fourier-transformed infrared spectroscopy (FTIR) measurements were carried out with the use of a Fourier Transform Infrared Spectrometer FSM 1201 Infraspek Ltd., (Russia). The sample for the investigation was prepared as a tablet with the addition of annealed KBr. The Raman spectra were recorded using an i-Raman Plus spectrometer (B&W Tek, Lubeck, Germany) at a laser excitation wavelength of 785 nm.

The diffuse reflectance spectra were measured on a UV-2600 spectrophotometer Shimadzu (Japan) equipped by the ISR-2600Plus attachment with an integrating sphere. The optical bandgap was estimated on the base of the measurements of diffuse reflectance spectra.

The thermal stability of lanthanum acetate was determined using thermogravimetry and differential scanning calorimetry on a TGA/DSC 3 + Mettler Toledo (Germany). The samples were heated from 30 to 600 °C in a corundum crucible at a rate of 10 °C/min in an oxidizing atmosphere with an air flow rate of 40 mL/min. The pyrolysis products were analyzed using the Agilent 7890B gas chromatograph equipped with a multifunctional pyrolyzer EGA/PY-3030D Shimadzu (Japan) from Frontier Laboratories, and the mass spectrometer with a single quadrupole mass analyzer Agilent 5977B GC/MS under programmed temperature conditions. The sample thermally decomposed at temperatures ranging from 150 to 650 °C at a heating rate of 15 °C/min in a helium flow. Fragmentary ions were analyzed in the mass range of

Table 1
Main processing and refinement parameters of the $La(CH_3COO)_3$ sample.

Compound	$La(CH_3COO)_3$	$La(CH_3COO)_3$ [25]
Form	Powder	Single crystal
Space group	$R\bar{3}$	$R\bar{3}$
a, Å	22.0164(1)	22.030(5)
c, Å	9.8718(1)	9.871(3)
V, Å^3	4143.99(6)	4148.78
Z	18	18
Rwp, %	2.94	2.25
Rp, %	2.30	2.65
χ^2	1.670	–
R(F^2)	7.77	–

15–550 *m/z* using full scan mode.

3. Results and discussion

A photo of the synthesized product is shown in Fig. 1(a). After evaporation, a loose clumpy powder of white color was obtained. XRD data are shown in Figs. 1(b) and S1. All peaks were successfully indexed by trigonal the unit cell (space group $R\bar{3}$) with parameters close to those previously reported for $La(CH_3COO)_3$ [25]. The refinement was stable and yielded low R-factors (Fig. 1, Table 1).

The monocrystal sample in the work of Meyer et al. [25] was obtained from the ammonia complex $(NH_4)_3[La(CH_3COO)_3]*0.5H_2O$ by recrystallization in a glass ampoule at 180 °C for two days. Despite differences in synthesis methods and the final form of the sample, the structural parameters of both the monocrystal and powdered sample obtained in this study are identical. Here it should be noted that compounds containing rare earth elements, including La, often exhibit a phenomenon known as polymorphism [38,39].

DTG, TG and DTA curves obtained on heating (in air) of $La(CH_3COO)_3$ up to 900 °C (at 10 °C/min) are shown in Fig. 2. The obtained results reveal that the decomposition process of the acetate begins around 300 °C and finishes at ≥700 °C, involving four (I–IV) thermal events of mass loss. Fig. 2 indicates that the total mass loss observed (48.4 %) closely aligns with the expected mass loss (48.45 %) for the transformation from $La(CH_3COO)_3$ to La_2O_3. To clarify the physicochemical nature of the thermal phenomena observed, it is essential to interpret the results of thermogravimetry and DTA, taking into account the identified composition of both solid and gas phase products formed throughout the entire decomposition process. Gas phase identification during the acetate decomposition was conducted using a gas chromatograph and mass spectrometer (Figs. S2 and S3). Mass spectrometric detection of the initial three thermal effects revealed identical decomposition products of the acetate group, namely acetone and carbon dioxide. The formation of acetone and CO_2 molecules arises from the pyrolytic decarboxylation process, wherein acetate groups undergo ketonization, yielding acetone and carbon dioxide (2 $La(CH_3COO)_3 \rightarrow La_2O_3 + 3\ (CH_3)_2CO_{(g)} + 3\ CO_{2\ (g)}$). Hydrolytic and pyrolytic activities account for the gradual mass loss observed along the sloping plateau (see Fig. 2), characterized by a lack of distinct steps, resulting in a substantial mass loss (40 %) attributed to the highly overlapping thermal events I-III. The fourth thermal effect (IV) is associated with the decomposition of $La_2O_2CO_3$ to La_2O_3 with the release of one molecule of carbon dioxide, which is consistent with the results of TG (7.14 %). According to XRD analysis, initial phase of La_2O_3 and phase after $La(CH_3COO)_3$ decomposition is the same (see Fig. S4).

Initial lattice constants and atomic coordinates (Table S1) of $La(CH_3COO)_3$ for DFT calculations were taken from work of Meyer et al. [25] and rhombohedral representation of crystal structure in *R*-3 space group presented in Fig. 3(a). As the experimental data for hydrogen atom coordinates were unavailable (not obtained experimentally), the hydrogen atoms were positioned within the cell around each non-oxygenated carbon atom. The DFT-optimized structure depicted in Fig. 3(b), along with related structural data, including the obtained atomic coordinates of hydrogen atoms, can be found in Table S2.

The experimental Raman and infrared spectra, as illustrated in Fig. 4, exhibit a multitude of spectral bands observed in both cases. Vibrational representation for the $La(CH_3COO)_3$ should be written as $\Gamma_{vibr} = 66A_g + 66E_g + 65A_u + 65E_u$, where the *g*-labeled modes Raman-active, while the *u*-labeled modes infrared-active. The acoustic modes are $A_u + E_u$. As can be seen from Fig. 4, vibrational spectra are consistent with the vibrational representation outlined above. The DFT calculated wavenumbers are presented in Fig. 4 as vertical ticks. According to the lattice dynamics calculation, region of vibrational spectra from 2900 to 3065 cm^{-1} related to C—H stretching vibrations. The symmetric-like stretching of CH_3 parts located from 2900 to 2935 cm^{-1}. The C—O stretching vibrations observed from 1525 to 1624 cm^{-1}. Spectral range of

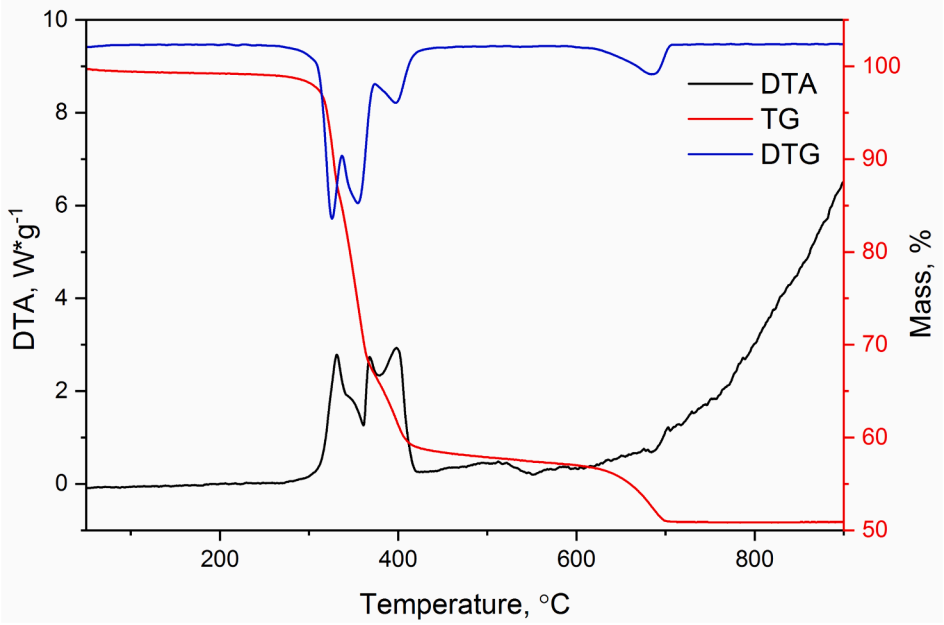

Fig. 2. Thermal analysis of $La(CH_3COO)_3$.

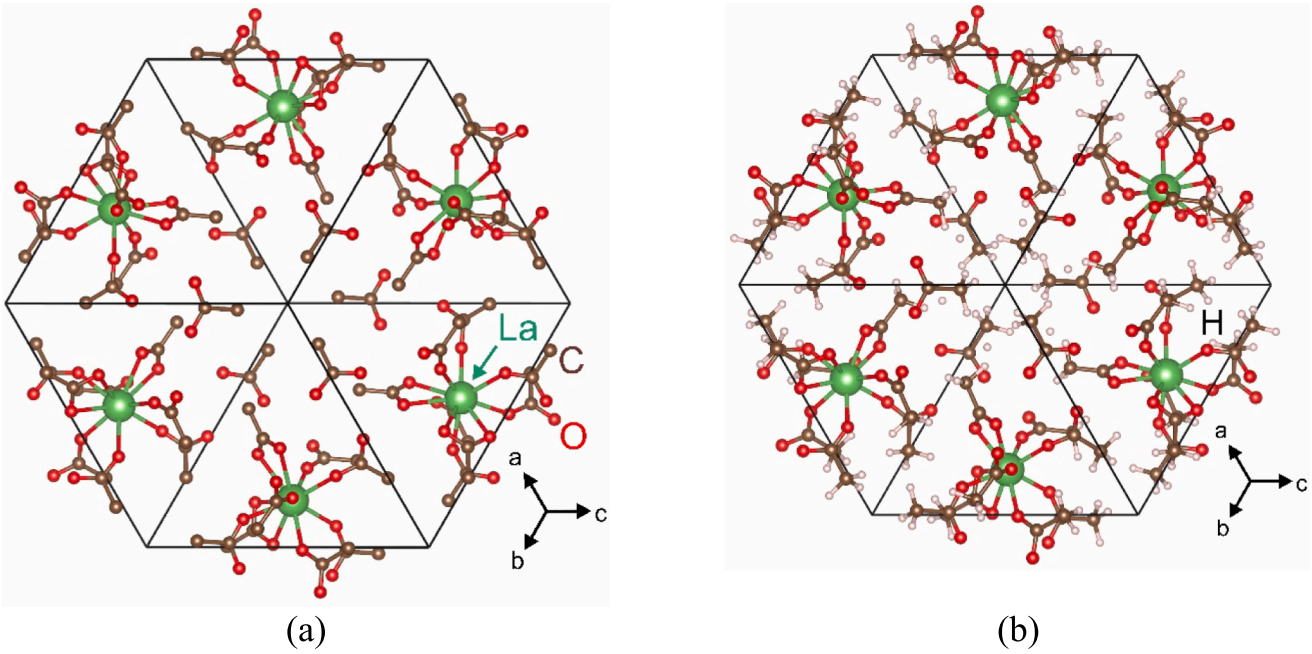

Fig. 3. Rhombohedral representation of $La(CH_3COO)_3$ structure based on experimental data (Table S1) (a) and DFT optimized structure with hydrogen atoms included in cell (Table S2) (b).

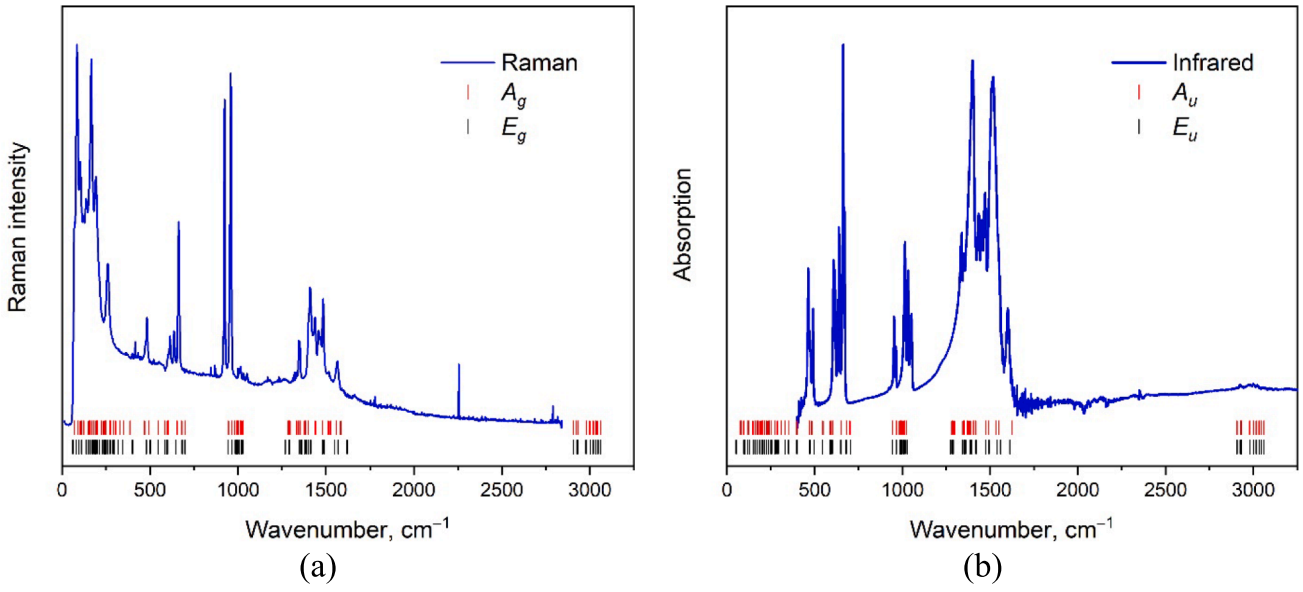

Fig. 4. Experimental Raman (a) and infrared (b) spectra from $La(CH_3COO)_3$. DFT calculated wavenumbers shown with vertical ticks.

1268–1479 cm^{-1} consist of C–O_2 stretching-like, C–O_2 stretching-like mixed with CH_3 deformations and pure deformational vibrations of CH_3 parts of CH_3COO molecules. The C—C bond vibrations appeared between 941 and 1027 cm^{-1}. Two strongest Raman bands (Fig. 4(a)) in this area can be attributed to symmetric stretching of CH_3COO molecule as a whole. The group of strong lines from 647 to 703 cm^{-1} related to combination of O and CH_3 movements. The medium band at 260 cm^{-1} in Raman spectrum associated with CH_3 rotations. The low-wavenumber part of spectra contains large number of vibrations with complex form.

Calculated electronic band structure for $La(CH_3COO)_3$ along high symmetry points of Brillouin zone using LDA approach is shown in Fig. 5 (a). Labels and coordinates of BZ selected points can be listed as Γ(0,0,0), L(0.5,0,0), T(0.5,−0.5,0.5), P_0(0.211,−0.788,0.211), P_2(0.211,0.211,0.211), F(0.5,−0.5,0) and chosen path can be found in Figs. S5 and 5(a). As can be seen in Fig. 5, $La(CH_3COO)_3$ is an indirect wide band gap semiconductor material with E_g equal to 4.19 eV. The top of valence band is located at the F point, while the bottom of conduction band is between P_2 and Γ points. Nevertheless, direct electronic transition (4.21 eV) is close to indirect, while the Γ–Γ transition is about 4.25 eV. According to the calculated total and partial electronic density of states (DOS), the top of the valence band is formed by the p-states of oxygen ions. The bottom of conduction band is formed by p-states of carbon ions. Thus, according to the calculation data, the charge transfer from oxygen to carbon ions within the molecular group O_2C–CH_4 is possible under irradiation of $La(CH_3COO)_3$ using a wavelength shorter than 296 nm (4.19 eV).

The optical diffuse reflectance spectrum recorded for the sample La $(CH_3COO)_3$ is shown in Fig. 6. The optical bandgap determined using the

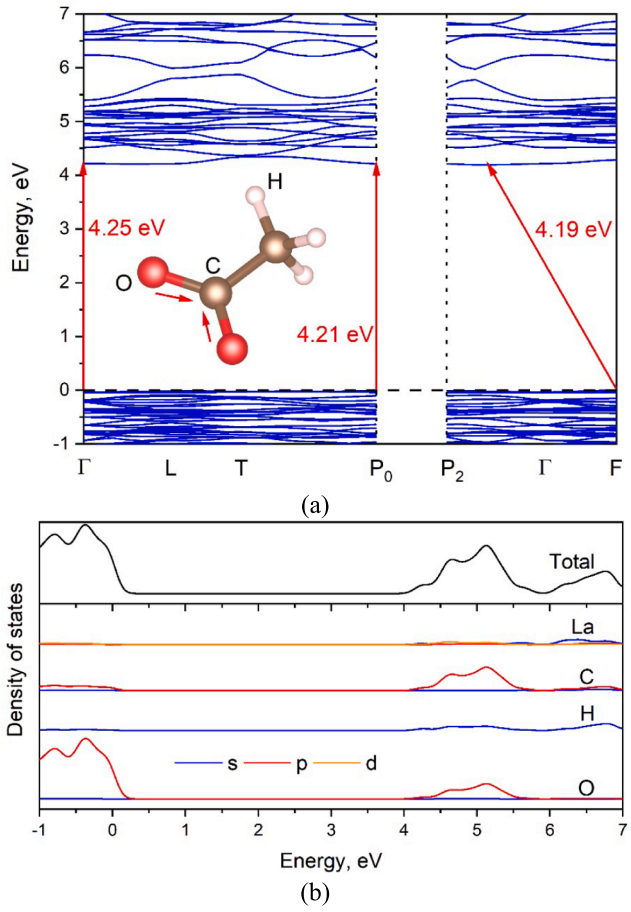

Fig. 5. Electronic band structure of $La(CH_3COO)_3$ calculated via LDA approximation.

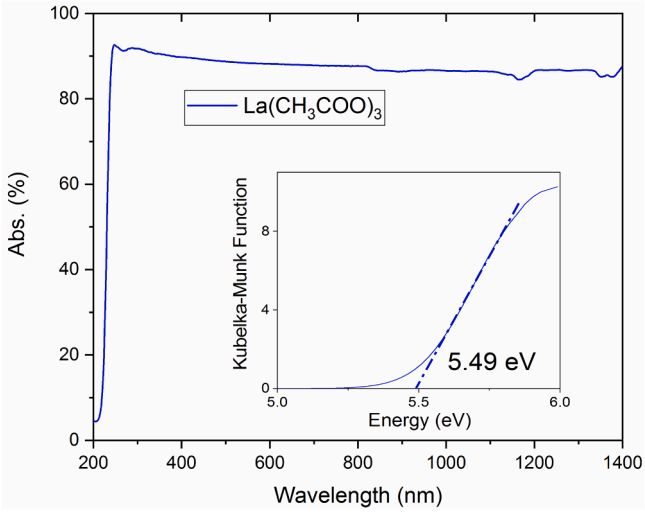

Fig. 6. Diffuse reflection UV–vis spectra of $La(CH_3COO)_3$.

Kubelka-Munk algorithm [40] is 5.49 eV. Thus, overcoming the optical bandgap is possible when irradiating $La(CH_3COO)_3$ with a wavelength shorter than 226 nm, which corresponds to the deep UV (DUV) region spanning between 280 nm and approximately 200 nm [41]. At the same time, it can be concluded that $La(CH_3COO)_3$ is optically transparent material across a wide range of wavelengths. Among other wide band gap materials with a similar electron transition energy, one can highlight diamond, $E_g = 5.47$ eV [42], hexagonal boron nitride, 5.96 eV [43], and β-Ga_2O_3, 4.8 eV [44].

As can be seen above, the difference between calculated and experimental band gap is about 1.3 eV. The underestimation of experimental values in DFT calculations using the LDA approximation is common, reflecting a well-known issue in DFT where band gaps are often underestimated [45–47].

4. Conclusions

In this study, lanthanum acetate ($La(CH_3COO)_3$) was successfully synthesized from high-purity reagents, with lanthanum oxide (La_2O_3) being dissolved in acetic acid (CH_3COOH) and water followed by evaporation at 150 °C. Structural characterization of the synthesized material was performed using X-ray powder diffraction (XRD). Heating of $La(CH_3COO)_3$ up to 900 °C in air revealed a decomposition process initiating around 300 °C and stops at ≥700 °C. This process involved four distinct thermal events (I–IV) of mass loss. Gas phase identification during acetate decomposition was performed using a gas chromatograph and mass spectrometer revealing identical decomposition products: acetone and carbon dioxide. Due to unavailable experimental data for hydrogen atom coordinates, the hydrogen atoms were positioned within the cell around each non-oxygenated carbon atom, and these atomic coordinates were successfully refined during the geometry optimization process. Raman and infrared spectra confirmed obtained structural model. $La(CH_3COO)_3$ is found to be an indirect wide band gap material, meanwhile, direct electronic transition is close to indirect. The optical diffuse reflectance spectrum showed an optical bandgap of 5.49 eV determined using the Kubelka-Munk algorithm. Overcoming the optical bandgap is possible when irradiating $La(CH_3COO)_3$ with a wavelength shorter than 226 nm, corresponding to the deep UV (DUV) region, thus, $La(CH_3COO)_3$ is optically transparent across a wide range of wavelengths, including visible part of spectra.

Declaration of competing interest

The authors declare that they have no known competing financial interests or personal relationships that could have appeared to influence the work reported in this paper.

Data availability

Data will be made available on request.

Acknowledgements

The work was partially carried out using the resources of the Research Resource Center “Natural Resources Management and Physico-Chemical Research” (Tyumen University) with financial support from the Ministry of Science and Higher Education of the Russian Federation (contract No. 05.594.21.0019., Unique identification number RFMEFI59420X0019). DFT calculations were carried out within the state assignment No FWES-2024-0003 of Kirensky Institute of Physics. The XRD work was carried out in accordance with the state assignment for the Institute of Solid State Chemistry of the Ural Branch of the Russian Academy of Sciences (No. 124020600024-5). The resources of the Research Park Computing Center and Center for Optical and Laser Materials Research of Saint-Petersburg State University were used.

Appendix A. Supplementary data

Supplementary data to this article can be found online at https://doi.org/10.1016/j.ica.2024.122310.

References

[1] K. Binnemans, P.T. Jones, B. Blanpain, T. Van Gerven, Y. Yang, A. Walton, M. Buchert, Recycling of rare earths: a critical review, J. Clean. Prod. 51 (2013) 1–22, https://doi.org/10.1016/j.jclepro.2012.12.037.

[2] C. Tunsu, M. Petranikova, M. Gergorić, C. Ekberg, T. Retegan, Reclaiming rare earth elements from end-of-life products: a review of the perspectives for urban mining using hydrometallurgical unit operations, Hydrometallurgy 156 (2015) 239–258, https://doi.org/10.1016/j.hydromet.2015.06.007.

[3] A.T. Lima, G.M. Kirkelund, F. Ntuli, L.M. Ottosen, Screening dilute sources of rare earth elements for their circular recovery, J. Geochem. Explor. 238 (2022) 107000, https://doi.org/10.1016/j.gexplo.2022.107000.

[4] X. Pierron, I.D. Williams, P.J. Shaw, Unlocking the value of stockpiled mobile handsets: a Delphi evaluation of factors influencing end of use, Detritus 18 (2022) 12, https://doi.org/10.31025/2611-4135/2022.15159.

[5] K.L. Nash, A review of the basic chemistry and recent developments in trivalent f-elements separations, Solvent Extract. Ion Exchange 11 (4) (1993) 729–768, https://doi.org/10.1080/07366299308918184.

[6] J. Song, T. Huang, H. Qiu, X. Niu, X.M. Li, Y. Xie, T. He, A critical review on membrane extraction with improved stability: potential application for recycling metals from city mine, Desalination 440 (2018) 18–38.

[7] Z. Li, T. Liang, K. Li, P. Wang, Exposure of children to light rare earth elements through ingestion of various size fractions of road dust in REEs mining areas, Sci. Total Environ. 743 (2020) 140432, https://doi.org/10.1016/j.scitotenv.2020.140432.

[8] H. Yang, F. Peng, D.E. Schier, S.A. Markotic, X. Zhao, A.N. Hong, X. Bu, Selective crystallization of rare-earth ions into cationic metal-organic frameworks for rare-earth separation, Angew. Chem. Int. Ed. 60 (20) (2021) 11148–11152.

[9] G.-J.-P. Deblonde, J.A. Mattocks, D.M. Park, D.W. Reed, C.J.A. Jr, Y. Jiao, Selective and efficient biomacromolecular extraction of rare-earth elements using lanmodulin, Inorg. Chem. 59 (17) (2020) 11855–11867, https://doi.org/10.1021/acs.inorgchem.0c01303.

[10] J.A. Cotruvo Jr, E.R. Featherston, J.A. Mattocks, J.V. Ho, T.N. Laremore, Lanmodulin: a highly selective lanthanide-binding protein from a lanthanide-utilizing bacterium, J. Am. Chem. Soc. 140 (44) (2018) 15056–15061.

[11] H. Singer, B. Drobot, C. Zeymer, R. Steudtner, L.J. Daumann, Americium preferred: lanmodulin, a natural lanthanide-binding protein favors an actinide over lanthanides, Chem. Sci. 12 (47) (2021) 15581–15587, https://doi.org/10.1039/D1SC04827A.

[12] T. Madanhire, H. Davids, M.C. Pereira, E.C. Hosten, A. Abrahams, Synthesis, characterisation and anticancer activity screening of lanthanide(III) acetate complexes with benzohydrazone and nicotinohydrazone ligands, Polyhedron 184 (2020) 114560, https://doi.org/10.1016/j.poly.2020.114560.

[13] Y.-B. Zhou, S.-J. Jin, Y. Cai, X. Teng, L. Chen, C.-S. Tang, Y.-F. Qi, Lanthanum acetate inhibits vascular calcification induced by vitamin D3 plus nicotine in rats, Exp. Biol. Med. (Maywood) 234 (8) (2009) 908–917, https://doi.org/10.3181/0811-RM-346.

[14] Y.U. Qiongyan, Z.H.O.U. Xiuxia, L.I.U. Maosheng, C.H.E.N. Jianqiao, Z.H.O.U. Zhengyuan, Y.I.N. Xia, C.A.I. Yuepeng, Syntheses, characterization, and luminescence of two lanthanide complexes $[Ln_2(acetate)_6(H_2O)_4]\cdot 4H_2O$ (Ln= Tb (1), Sm (2)), J. Rare Earths 26 (2) (2008) 178–184.

[15] F. Hussain, S. Sandriesser, M. Speldrich, G.R. Patzke, A new series of lanthanoid containing Keggin-type germanotungstates with acetate chelators: $[\{Ln(CH_3COO)GeW_{11}O_{39}(H_2O)\}_2]^{12-}$ {Ln=Eu^{III}, Gd^{III}, Tb^{III}, Dy^{III}, Ho^{III}, Er^{III}, Tm^{III}, and Yb^{III}}, J. Solid State Chem. 184 (1) (2011) 214–219, https://doi.org/10.1016/j.jssc.2010.11.005.

[16] S.M.R. da Rocha, C.A. da Silva Queiroz, A. Abrão, Synthesis and characterization of lanthanum acetate for application as a catalyst, J. Alloy. Compd. 344 (1) (2002) 389–393, https://doi.org/10.1016/S0925-8388(02)00391-2.

[17] Z. Jiang, T. Su, C. Chua, L.K. Ang, C. Zhang, L. Cao, Y.S. Ang, Lanthanum oxyhalide monolayers: an exceptional dielectric companion to 2-D semiconductors, IEEE Trans. Electron. Devices 70 (4) (2023) 1509–1519, https://doi.org/10.1109/TED.2023.3236903.

[18] A.S. Oreshonkov, N.O. Azarapin, N.P. Shestakov, S.V. Adichtchev, Experimental and DFT study of $BaLaCuS_3$: direct band gap semiconductor, J. Phys. Chem. Solid 148 (2021) 109670, https://doi.org/10.1016/j.jpcs.2020.109670.

[19] A.V. Gavrikov, P.S. Koroteev, Z.V. Dobrokhotova, A.B. Ilyukhin, N.N. Efimov, D. I. Kirdyankin, M.A. Bykov, M.A. Ryumin, V.M. Novotortsev, Novel heterometallic polymeric lanthanide acetylacetonates with bridging cymantrenecarboxylate groups – synthesis, magnetism and thermolysis, Polyhedron 102 (2015) 48–59, https://doi.org/10.1016/j.poly.2015.07.063.

[20] A.F. Mohd Abd Fatah, A.Z. Rosli, A.A. Mohamad, A. Muchtar, N.A. Hamid, Electrochemical evaluation of nickel oxide addition toward lanthanum strontium cobalt ferrite cathode for intermediate temperature solid oxide fuel cell (IT-SOFCS), Energies 15 (14) (2022) 5188, https://doi.org/10.3390/en15145188.

[21] S.D. Safian, N.I. Abd Malek, Z. Jamil, S.-W. Lee, C.-J. Tseng, N. Osman, Study on the surface segregation of mixed ionic-electronic conductor lanthanum-based perovskite oxide $La_{1-x}Sr_xCo_{1-y}Fe_yO_{3-\delta}$ materials, Int. J. Energy Res. 46 (6) (2022) 7101–7117, https://doi.org/10.1002/er.7733.

[22] J. Yu, L. Hu, J. Ren, Clarifying the different roles of rare earth ions in the crystallization of upconversion oxyfluoride glass ceramics by solid-state nuclear magnetic resonance spectroscopy, Inorg. Chem. 60 (5) (2021) 3401–3409, https://doi.org/10.1021/acs.inorgchem.0c03804.

[23] Y. Xie, L. Wang, P. Ning, X. Wang, Q. Wang, Y. Zhang, M. Wang, Superior activity of Ce-HZSM-5 catalyst for catalytic oxidation of arsine at low oxygen, Appl. Organomet. Chem. 33 (3) (2019) e4745, https://doi.org/10.1002/aoc.4745.

[24] Q. Liu, M. Xu, Z.-X. Low, W. Zhang, F. Tao, F. Liu, N. Liu, Controlled synthesis of pyrochlore $Pr_2Sn_2O_7$ nanospheres with enhanced gas sensing performance, RSC Adv. 6 (26) (2016) 21564–21570, https://doi.org/10.1039/C5RA26028K.

[25] G. Meyer, D. Gieseke-Vollmer, Das wasserfreie lanthanacetat, $La(CH_3COO)_3$, und sein precursor, $(NH_4)_3[La(CH_3COO)_6]\cdot 1/2\ H_2O$: synthese, strukturen, thermisches verhalten, Z. Anorg. Allg. Chem. 619 (9) (1993) 1603–1608, https://doi.org/10.1002/zaac.19936190916.

[26] A. Lossin, G. Meyer, $Pr(CH_3COO)_3$, ein wasserfreies Selten-Erd-Acetat mit Netzwerkstruktur, Z. Anorg. Allg. Chem. 620 (3) (1994) 438–443, https://doi.org/10.1002/zaac.19946200306.

[27] S. Gomez Torres, G. Meyer, Anhydrous neodymium(III) acetate, Z. Anorg. Allg. Chem. 634 (2) (2008) 231–233, https://doi.org/10.1002/zaac.200700407.

[28] A. Lossin, G. Meyer, Wasserfreie Selten-Erd-Acetate, $M(CH_3COO)_3$ (M = Sm·Lu, Y) mit Kettenstruktur. Kristallstrukturen von $Lu(CH_3COO)_3$ und $Ho(CH_3COO)_3$, Z. Anorg. Allg. Chem. 619 (9) (1993) 1609–1615, https://doi.org/10.1002/zaac.19936190917.

[29] H. Kataoka, S. Takeda, N. Nakamura, 45Sc nuclear magnetic resonance and phase transitions in scandium acetates, $Sc(CH_3COO)_3$ and $Sc(CD_3COO)_3$, J. Phys. Soc. Jpn. 62 (5) (1993) 1478–1481, https://doi.org/10.1143/JPSJ.62.1478.

[30] G.A.M. Hussein, Spectrothermal investigation of the decomposition course of lanthanum acetate hydrate, J. Therm. Anal. 42 (6) (1994) 1091–1102, https://doi.org/10.1007/BF02546919.

[31] I. Mayer, F. Kassierer, A thermogravimetric study of the lighter rare earth acetates, J. Inorg. Nucl. Chem. 28 (10) (1966) 2430–2432, https://doi.org/10.1016/0022-1902(66)80147-1.

[32] K.C. Patil, G.V. Chandrashekhar, M.V. George, C.N.R. Rao, Infrared spectra and thermal decompositions of metal acetates and dicarboxylates, Can. J. Chem. 46 (2) (1968) 257–265, https://doi.org/10.1139/v68-040.

[33] B.H. Toby, EXPGUI, a graphical user interface for GSAS, J. Appl. Cryst. 34 (2) (2001) 210–213.

[34] S.J. Clark, M.D. Segall, C.J. Pickard, P.J. Hasnip, M.I.J. Probert, K. Refson, M. C. Payne, First principles methods using CASTEP, Zeitschrift Für Kristallographie – Cryst. Mater. 220 (2005) 567–570, https://doi.org/10.1524/zkri.220.5.567.65075.

[35] G.P. Srivastava, D. Weaire, The theory of the cohesive energies of solids, Adv. Phys. 36 (1987) 463–517, https://doi.org/10.1080/00018738700101042.

[36] J.P. Perdew, A. Zunger, Self-interaction correction to density-functional approximations for many-electron systems, Phys. Rev. B 23 (1981) 5048–5079, https://doi.org/10.1103/PhysRevB.23.5048.

[37] D.M. Ceperley, B.J. Alder, Ground state of the electron gas by a stochastic method, Phys. Rev. Lett. 45 (1980) 566–569, https://doi.org/10.1103/PhysRevLett.45.566.

[38] M. Zinkevich, Thermodynamics of rare earth sesquioxides, Prog. Mater. Sci. 52 (4) (2007) 597–647, https://doi.org/10.1016/j.pmatsci.2006.09.002.

[39] J. Felsche, Polymorphism and crystal data of the rare-earth disilicates of type $RE_2Si_2O_7$, J. Less Common Met. 21 (1) (1970) 1–14, https://doi.org/10.1016/0022-5088(70)90159-1.

[40] R. Alcaraz de la Osa, I. Iparragirre, D. Ortiz, J.M. Saiz, The extended Kubelka-Munk theory and its application to spectroscopy, ChemTexts 6 (1) (2019) 2, https://doi.org/10.1007/s40828-019-0097-0.

[41] P.S. Halasyamani, W. Zhang, Viewpoint: inorganic materials for UV and deep-UV nonlinear-optical applications, Inorg. Chem. 56 (20) (2017) 12077–12085, https://doi.org/10.1021/acs.inorgchem.7b02184.

[42] H. Yang, Y. Ma, Y. Dai, Progress of structural and electronic properties of diamond: a mini review, Functional Diamond 1 (1) (2022) 150–159, https://doi.org/10.1080/26941112.2021.1956287.

[43] D.A. Evans, A.G. McGlynn, B.M. Towlson, M. Gunn, D. Jones, T.E. Jenkins, R. Winter, N.R.J. Poolton, Determination of the optical band-gap energy of cubic and hexagonal boron nitride using luminescence excitation spectroscopy, J. Phys.: Condens. Matter 20 (7) (2008) 075233, https://doi.org/10.1088/0953-8984/20/7/075233.

[44] L.K. Ping, D.D. Berhanuddin, A.K. Mondal, P.S. Menon, M.A. Mohamed, Properties and perspectives of ultrawide bandgap Ga2O3 in optoelectronic applications, Chin. J. Phys. 73 (2021) 195–212, https://doi.org/10.1016/j.cjph.2021.06.015.

[45] J.P. Perdew, Density functional theory and the band gap problem, Int. J. Quantum Chem. 28 (S19) (1985) 497–523, https://doi.org/10.1002/qua.560280846.

[46] A.S. Oreshonkov, E.M. Roginskii, A.S. Krylov, A.A. Ershov, V.V.N. Structural, Electronic and vibrational properties of LaF_3 according to density functional theory and Raman spectroscopy, J. Phys.: Condens. Matter 30 (25) (2018) 255901, https://doi.org/10.1088/1361-648X/aac452.

[47] A.S. Oreshonkov, E.M. Roginskii, V.V. Atuchin, New candidate to reach Shockley-Queisser limit: the DFT study of orthorhombic silicon allotrope Si(oP32), J. Phys. Chem. Solid 137 (2020) 109219, https://doi.org/10.1016/j.jpcs.2019.109219.